Inorganic Chemistry

Article

pubs.acs.org/IC

Half-Integer Spin Heptanuclear Single-Molecule Magnet with an Unusual $Mn^{III}_6Mn^{II}$ Exchange-Coupled Core

Siou-Yin Chen,[†] Christopher C. Beedle,[‡] Pei-Rung Gan,[†] Gene-Hsian Lee,[§] Stephen Hill,*[,‡,∇] and En-Che Yang*[,†]

[†]Department of Chemistry, Fu Jen Catholic University, Hsinchuang, Taipei, 24205, Taiwan, Republic of China

[‡]National High Magnetic Field Laboratory, Florida State University, 1800 E. Paul Dirac Drive, Tallahassee, Florida 32310, United States

[§]Instrumentation Centre, College of Science, National Taiwan University, Taipei, 106, Taiwan, Republic of China

[∇]Department of Physics, Florida State University, Tallahassee, Florida 32310, United States

Supporting Information

ABSTRACT: The synthesis, X-ray crystallography, magnetic properties, and high-field electron paramagnetic resonance (HFEPR) of a new heptanuclear manganese complex $[Mn_7(heamp)_6](ClO_4)_2{\cdot}4CH_2Cl_2{\cdot}H_2O$ (complex **2**), in which $heampH_3$ is 2-[*N*,*N*-di(2-hydroxyethyl)aminomethyl]phenol (compound **1**), is reported. Complex **2** has a hexagonal, disk-shaped topology and contains six Mn(III) ions and a central Mn(II) ion. It crystallizes in the monoclinic space group $P2_1/c$ with two molecular orientations. Consideration of the cluster topology, together with variable-temperature and variable-field DC magnetic susceptibility data, suggest that complex **2** exists in a half-integer, $S = {}^{19}/_2 \pm 1$ spin ground state, with appreciable uniaxial zero-field splitting ($D = -0.16$ cm^{-1}). AC magnetic susceptibility measurements clearly show out-of-phase signals, which are frequency- and temperature-dependent, indicating slow magnetization relaxation behavior. An analysis of the relaxation data employing the Arrhenius formula yielded an effective relaxation barrier of 12.9 cm^{-1}. Simulations of HFEPR studies agree with the assignment of an $S \approx {}^{19}/_2$ spin ground state, with $g = 1.96$, $D = -4.71$ GHz (-0.16 cm^{-1}), and a longitudinal fourth-order zero-field splitting parameter $B_4^0 = -2.7 \times 10^{-4}$ GHz (-9.0×10^{-6} cm^{-1}).

INTRODUCTION

Manganese-based metal clusters that incorporate phenol groups are attractive, not only because they can be functionalized, thus leading to new and interesting topologies, but also because they can function as important reactive sites in nature.[1] An excellent example of this is the tetranuclear manganese cluster that drives the catalytic activity in photosystem II. In addition, manganese can exist in many oxidation states; this imparts synthetic flexibility, which can lead to new molecular topologies and interesting magnetic properties. Single-molecule magnets (SMMs)[2] are an extremely interesting class of exchange coupled transition-metal clusters that exhibit slow magnetization relaxation behavior and, because of their unique size, shape, and anisotropy, SMMs provide a unique platform for the study of molecular systems that possess both classic magnetic properties and quantum properties. In addition, SMMs have attracted considerable attention in the fields of molecular spintronics[3] and quantum computation and quantum information storage.[4] In the past two decades, extensive investigations of SMMs have yielded some benchmark findings including: quantum tunneling of magnetization (QTM),[5] quantum phase interference (QPI),[6] exchange bias,[7] spin-parity effects,[8] and quantum coherence/decoherence.[9]

Disk-shaped heptanuclear manganese clusters are a very interesting subset of SMMs, because they are synthetically flexible.[10−18] The topologies of the exchange coupled cores of these complexes are almost identical. However, by strategically changing peripheral organic ligands, e.g., diketonates, functionalized pyridyls, diethanolamines, etc., the oxidation states and the nature of the magnetic exchange interactions can be manipulated to produce complexes with both integer- and half-integer spin ground states that fall into three general groups: $Mn^{II}_4Mn^{III}_3$,[10−14] Mn^{II}_7,[15] and $Mn^{II}_3Mn^{III}_4$.[16−18] Few systems offer such diverse synthetic options, which makes the studies of Mn_7 complexes interesting from a fundamental viewpoint.

In previous studies, we reported on the synthesis of pyridyl-containing and phenol-containing ligands for use in forming metal clusters that show slow magnetization relaxation (SMM-like) phenomena.[19] In the present study, a new phenol-containing diethanolamine ligand, 2-[*N*,*N*-di(2-hydroxyethyl)aminomethyl]phenol ($heampH_3$, see Scheme 1),

Scheme 1. Synthesis of $heampH_3$ (Compound 1)

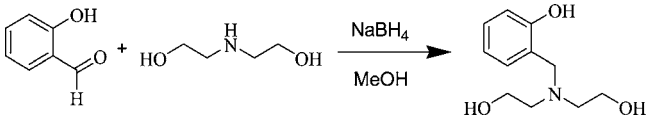

was synthesized and was used in combination with $[Mn_3O(O_2CMe)_6(py)_3](ClO_4)$[20] to produce a new hepatanuclear manganese SMM, $[Mn_7(heamp)_6](ClO_4)_2{\cdot}4CH_2Cl_2{\cdot}H_2O$ (complex **2**), with a unique electronic arrangement $Mn^{II}Mn^{III}_6$.

Received: September 1, 2011
Published: April 3, 2012

   dx.doi.org/10.1021/ic2019154 | *Inorg. Chem.* 2012, 51, 4448−4457

Crystallography, magnetometry, and electron paramagnetic resonance were used to study this interesting half-integer spin SMM.

EXPERIMENTAL SECTION

Synthesis. All chemicals and solvents were used as received without any additional purification. The synthesis of $[Mn_3O(O_2CMe)_6(py)_3](ClO_4)$ has been reported previously.[20]

2-[*N*,*N*-di(2-hydroxyethyl)aminomethyl]phenol (heampH$_3$) (Compound 1). A solution of diethanolamine (4.2 g, 40 mmol) in 15 mL of methanol and a solution of salicylaldehyde (4.88 g, 40 mmol) in 15 mL of methanol were combined and stirred under a nitrogen atmosphere for 2 h. To the resulting solution, a mixture of $NaBH_4$ (1.51 g, 40 mmol) in 10 mL of methanol was added dropwise while in an ice bath, after which the solution was stirred for another hour. The methanol was removed by decantation and replaced by water. The resulting solution was neutralized with glacial acetic acid, the solution extracted by CH_2Cl_2 (30 mL × 3), and dried on $MgSO_4$. Analytically pure heampH$_3$ was obtained by elution from a silica-gel column with EA/hexane = 1/3 solution. Yield: 14.3%. (^{1}H NMR in $CDCl_3$, 300 MHz) δ: 2.78 (t, 4H, NCH_2CH$_2$), 3.76 (t, 4H, CH$_2$OH), 3.86 (s, 2H, CCH$_2$N), 6.77, 6.81, 7.00, 7.15 (dd, td, dd, td, 4H, phenyl-*H*). ^{13}C (75 MHz) δ: 56.2, 59.4, 60.1, 116.4, 119.5, 122.3, 128.9, 129.1, 157.4. Selected IR data (ATR-IR, cm^{-1}): 3369 (vs), 2952 (s), 2884 (s), 1613 (m), 1590 (s), 1490 (s), 1456 (s), 1408 (m), 1366 (m), 1256 (s), 1151 (m), 1138 (m), 1076 (m), 1033 (s) 758 (s). Anal. Calcd. for ($C_{11}H_{17}NO_3$): C, 62.54; H, 8.11; N, 6.63%. Found: C, 62.50; H, 8.10; N, 6.47%. HRESI-MS [M+H]$^+$: 212.1269 (calc.: 212.1287).

[Mn$_7$(heamp)$_6$](ClO$_4$)$_2$·4CH$_2$Cl$_2$·H$_2$O (Complex 2). To $[Mn_3O(O_2CMe)_6(py)_3](ClO_4)$ (2.63 g, 3.02 mmol) in 30 mL of CH_2Cl_2 was added heampH$_3$ (1.64 g, 7.76 mmol) in 30 mL of CH_2Cl_2. The mixture was stirred under aerobic conditions for 24 h and a dark brown solid was obtained. The solids were washed with CH_2Cl_2 and then dissolved in acetonitrile. Crystals were obtained after one week via diethylether diffusion. The crystals were collected and redissolved in CH_2Cl_2 and layered with hexanes, yielding X-ray diffraction (XRD)-quality crystals. Yield: 2.0%. Selected IR data (ATR-IR, cm^{-1}): 2878 (m), 1595 (m), 1476 (m), 1452 (m), 1199 (vs), 1126 (m), 1042 (m), 970 (vs), 902 (s), 761 (m). Anal. Calcd. for ($C_{66}H_{84}Cl_2Mn_7N_6O_{26}$): C, 43.25; H, 4.62; N, 4.59%. Found: C, 43.55; H, 4.70; N, 4.21%.

X-ray Structure Determination. A dark-brown crystal of complex **2**, with dimensions of 0.28 mm × 0.25 mm × 0.06 mm, was selected for X-ray analysis, which was carried out on a Bruker SMART CCD diffractometer, using Mo Kα radiation (λ = 0.71073 Å). The temperature of the crystal was controlled by means of an Oxford Cryosystems Cryostream Cooler. The detector was 5.00 cm from the crystal. The crystallographic data were collected over a hemisphere of reciprocal space, via a combination of three sets of exposures. Each set had a different φ angle, and each exposure of 5 s covered 0.30° in ω. An empirical absorption was made, based on the symmetry-equivalent reflections and the data were integrated using the *SADABS* program.[21] The structure was analyzed using the SHELXTL program on a personal computer (PC). The structure was solved using the Shelxs-97 program[22] and refined by the Shelxl-97 program[23] with full-matrix least-squares on F^2 values. The non-hydrogen atoms were refined anisotropically. Hydrogen atoms were fixed at the calculated positions and refined using a riding mode. Detailed crystallographic parameters are listed in Table 1.

Physical Measurements. The DC magnetic susceptibility data were collected with a Quantum Design MPMS7 system. Samples of **2** were finely ground and restrained with eicosane to prevent torquing of the crystallites. The variable-field and variable-temperature magnetic susceptibility data were also corrected for the gel capsule, sample rod, and eicosane backgrounds. Diamagnetic contributions to the susceptibility were estimated from Pascal's constants. DC susceptibility measurements and elemental analysis experiments were carried out at the Instrumentation Centre, National Taiwan University.

Table 1. Crystallographic Data for Complex 2

parameter	value
formula	$C_{70}H_{94}Cl_{10}Mn_7N_6O_{27}$
formula weight, Fw	2190.59 g mol^{-1}
temperature, T	150(2) K
space group	$P2_1/c$
a	14.9810(8) Å
b	22.1533(12) Å
c	13.1267(7) Å
α	90°
β	100.9372(13)°
γ	90°
volume, V	4277.3(4) Å^3
Z', Z	0.5, 2
F(000)	2234
density (calcd) mg m^{-3}	1.701
absorption coefficient	1.392 mm^{-1}
absorption correction	semiempirical from equivalents
reflns, measured	32721
reflns, independent	9819 [R(int) = 0.0700]
data/restraints/parameters	9819/6/544
goodness-of-fit on F^2	1.049
R indices [$I > 2\sigma(I)$]	$R1$ = 0.0648, $wR2$ = 0.1374
R indices (all data)	$R1$ = 0.0926, $wR2$ = 0.1499

High-field powder EPR data were collected at the U.S. National High Magnetic Field Laboratory Electron Magnetic Resonance facility, using a transmission probe in which microwaves are propagated through cylindrical lightpipes. High-frequency microwaves were generated by a phase-locked Virginia Diodes solid-state source operating at 13 ± 1 GHz, followed by a chain of multipliers and amplifiers. High magnetic fields were provided by a 17 T superconducting magnet.[24]

RESULTS AND DISCUSSION

Structure Description. Single-crystal X-ray data and refinement parameters for complex **2** are listed in Table 1. Complex **2** crystallizes in the monoclinic space group $P2_1/c$ with Z' = 0.5 and Z = 2. The asymmetric unit consists of one-half of a molecule with the other half generated by the symmetry equivalent transformations: $-x$, $-y$, $-z$, and the second molecule in the unit cell is related by a *c*-glide (x, $^1/_2 - y$, $^1/_2 + z$), yielding two independent molecular orientations in the unit cell. An ORTEP drawing of complex **2** is shown in Figure 1a.

The metal framework of compound **2** consists of a central Mn^{II} ion that is encircled by six Mn^{III} ions that form a roughly hexagonal disk. Oxidation-state determinations were based on charge considerations, bond-valence sum analysis (BVS)[25] (see the Supporting Information) and crystallographic evidence for Jahn−Teller elongated axes on six of the Mn ions. All seven of the metal ions are six-coordinated and exhibit distorted octahedral geometries. Mn−O bond lengths for the central Mn ion range between 2.173 Å and 2.199 Å and are consistent with a high-spin d^5 Mn^{II} ion. The other six Mn ions have four Mn−O bond lengths that range between 1.840−2.018 Å with two axially oriented Mn−O, Mn−N bonds that range between 2.180 Å and 2.300 Å, which is indicative of tetragonally elongated, high-spin d^4 Mn^{III} centers. The orientations of the six Jahn−Teller axes, shown in black, are presented in Figure 1b, and selected bond lengths are listed in Table 2. The Jahn−Teller axes lie along O−Mn−N bonds and are highly distorted. The central Mn^{II} ion and four of the Mn^{III} ions lie in the same molecular plane, while the remaining two Mn^{III} ions (Mn(4 and 4a)) lie 7.84° above and below the molecular plane, respectively

dx.doi.org/10.1021/ic2019154 | *Inorg. Chem.* 2012, 51, 4448−4457

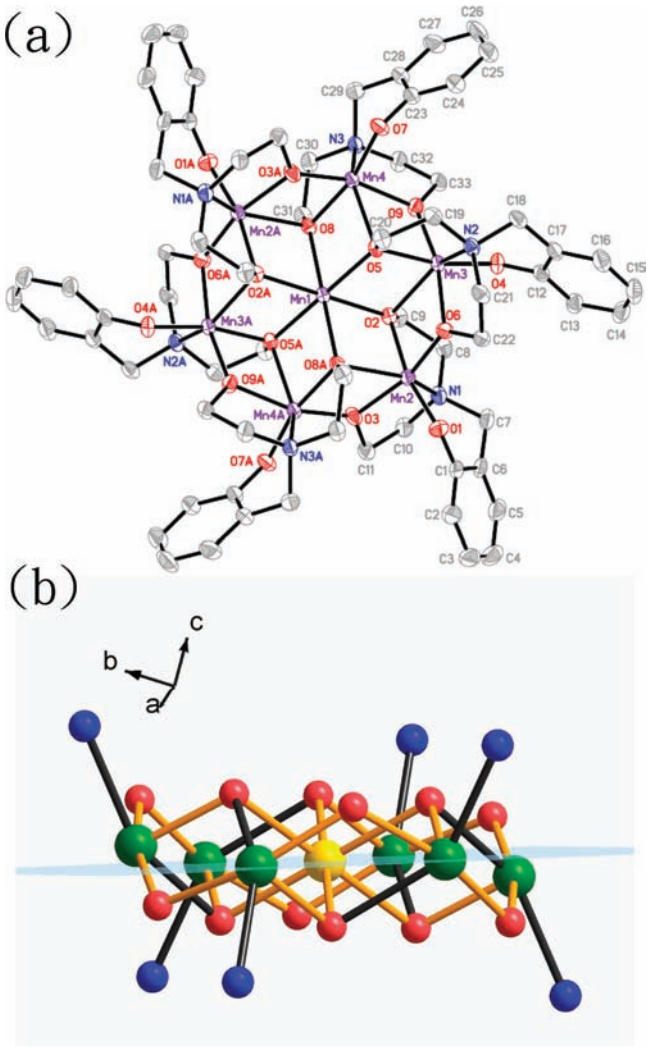

Figure 1. (a) ORTEP plot of $[Mn_7(heamp)_6]^{2+}$ (**2**) at the 50% probability level. Color scheme: Mn, purple; O, red; N, blue; C, gray. (b) Skeleton of **2**: Mn^{3+}, green; Mn^{2+}, yellow; O, red; N, blue. The Jahn–Teller axes of Mn^{3+} ions are represented by black sticks.

Table 2. Selected Metal–Ligand Bond Lengths in Complex 2[a]

metal–ligand pair	bond length (Å)	metal–ligand pair	bond length (Å)
Mn(1)–O(2)#1	2.173(3)	Mn(3)–O(4)	1.850(3)
Mn(1)–O(2)	2.173(3)	Mn(3)–O(9)	1.919(3)
Mn(1)–O(5)#1	2.185(3)	Mn(3)–O(5)	1.966(3)
Mn(1)–O(5)	2.185(3)	Mn(3)–O(6)	1.983(3)
Mn(1)–O(8)#1	2.199(3)	Mn(3)–N(2)	2.202(3)
Mn(1)–O(8)	2.199(3)	Mn(3)–O(2)	2.280(3)
Mn(2)–O(1)	1.840(3)	Mn(4)–O(7)	1.841(3)
Mn(2)–O(6)	1.917(3)	Mn(4)–O(3)#1	1.938(3)
Mn(2)–O(2)	1.966(3)	Mn(4)–O(8)	1.961(3)
Mn(2)–O(3)	1.987(3)	Mn(4)–O(9)	2.018(3)
Mn(2)–N(1)	2.199(4)	Mn(4)–N(3)	2.180(3)
Mn(2)–O(8)#1	2.285(3)	Mn(4)–O(5)	2.300(3)

[a]Symmetry transformations used to generate equivalent atoms: #1: $-x+1, -y+1, -z+3$; #2: $-x+1, -y+1, -z+2$.

(see Figure 1b). Intercluster Mn^{II}–Mn^{III} and Mn^{III}–Mn^{III} distances are 3.212–3.236 Å and 3.215–3.263 Å, respectively.

Six trianionic $heamp^{3-}$ tetradentate ligands act as bridges between neighboring metal centers and complete the coordination sphere of each molecule. The two ethoxy-oxygens and the phenolic-oxygen of each $heamp^{3-}$ ligand function as magnetic exchange pathways and are arranged in μ_3-O^-, μ_2-O^-, and μ-O^- coordination modes, respectively. Each of the six μ_2-O^- atoms bridge two neighboring Mn^{III} ions with bond angles of 111.00°, 111.91°, and 110.24°, with three inversion symmetry equivalents. The six μ_3-O^- atoms bridge two adjacent Mn^{III} ions and the central Mn^{II} ion forms a triangle with the oxo-atom out of the plane formed by the three Mn ions. Mn^{II}–μ_3-O–Mn^{III} bond angles range between 91.47° and 101.96° and Mn^{III}–μ_3-O–Mn^{III} angles range between 98.13° and 99.46°. The phenolic-oxygen and the nitrogen center of each of the $heamp^{3-}$ ligands complete the coordination sphere and cap the six peripheral Mn^{III} ions of the $[Mn^{II}Mn^{III}{}_6O_{18}]^{2+}$ magnetic core.

DC Magnetic Susceptibility Studies. Variable-temperature DC magnetic susceptibility measurements were collected on a polycrystalline sample of **2** with an applied magnetic field of 1 kG in the temperature range of 5–300 K; these are presented in Figure 2 in the form of a plot of $\chi_M T$ vs T. The

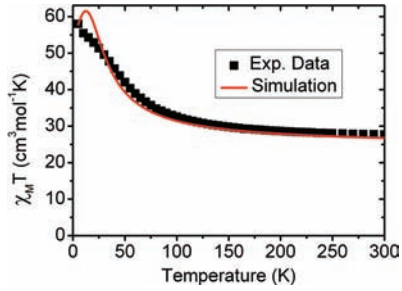

Figure 2. Plot of $\chi_M T$ versus T of complex **2** measured in a 1 kG magnetic field. The solid red line represents a theoretical simulation of the experimental data.

value of the $\chi_M T$ product is 27.7 cm^3 mol^{-1} K at 300 K, which is slightly higher than the spin-only value of 22.4 cm^3 mol^{-1} K expected for six noninteracting Mn^{III} ions and one Mn^{II} ion. This suggests that intracluster magnetic exchange interactions, presumably with ferrimagnetic arrangements, are active, even at room temperature. As the temperature is reduced to 90 K, the $\chi_M T$ product steadily increases to 33.6 cm^3 mol^{-1} K and then rapidly increases to 58.0 cm^3 mol^{-1} K at temperatures down to 5 K.

In order to gain insight into the nature of the magnetic exchange interactions within the molecule, simulations of the $\chi_M T$ versus T data were performed. A precise parametrization of the magnetic coupling in **2** requires six independent exchange constants: three Mn^{II}–Mn^{III} and three Mn^{III}–Mn^{III}. However, it is well-established that such an approach involves way too many parameters, not to mention the fact that it neglects anisotropic zero-field splitting interactions that are known to influence the analysis at lower temperatures. In essence, the information content within the $\chi_M T$ versus T curve simply does not adequately constrain a model with six adjustable parameters.[26] Nevertheless, it is instructive to employ a simplified two-J model, which treats the molecule as an approximately regular hexagon, where J_1 and J_2 represent Mn^{II}–O–Mn^{III} and Mn^{III}–O–Mn^{III} exchange pathways, respectively (see Figure 3). It should be stressed that, although this represents a major oversimplification, it can provide us with useful insights. Moreover, as we shall see later, such a simplification is reasonably consistent with expectations in terms of the type of (ferromagnetic or antiferromagnetic) exchange interactions within the molecule. The simplified exchange model leads to the following Heisenberg

dx.doi.org/10.1021/ic2019154 | Inorg. Chem. 2012, 51, 4448–4457

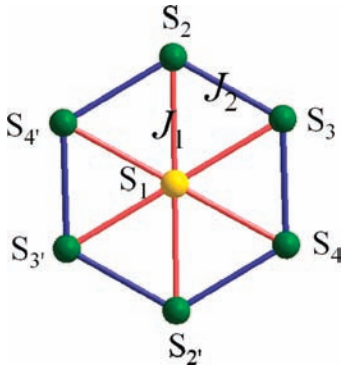

Figure 3. Plot showing a simplified magnetic exchange coupling scheme for complex **2**, where J_1 = Mn^{II}–O–Mn^{III} exchange pathways, and J_2 = Mn^{III}–O–Mn^{III} exchange pathways.

spin Hamiltonian, where J_1 and J_2 are exchange constants and S_i are spin operators:[27]

$$\hat{H} = -2J_1(S_1\cdot S_2 + S_1\cdot S_3 + S_1\cdot S_4 + S_1\cdot S_{2'} + S_1\cdot S_{3'} + S_1\cdot S_{4'}) - 2J_2(S_2\cdot S_3 + S_3\cdot S_4 + S_4\cdot S_{2'} + S_{2'}\cdot S_{3'} + S_{3'}\cdot S_{4'} + S_{4'}\cdot S_2) \quad (1)$$

Simulations of the variable-temperature DC magnetic susceptibility were performed using the program MAGPACK.[28] The best simulation, shown as a red solid line in Figure 2, yielded the parameters J_1 = −0.26 cm^{-1}, J_2 = 3.0 cm^{-1}, and g = 2.1. This result makes reasonable sense, in terms of the structure of the core, as we now outline. The ferromagnetic coupling among the six Mn^{III} ions (J_2 > 0) on the ring is analogous to that reported for the complex $[NaMn^{III}_6(OMe)_{12}(dbm)_6]BPh_4$, where the six Mn^{III} ions are ferromagnetically coupled to give an S = 12 ground state.[29a] A search of the literature further indicates that this ferromagnetic coupling can be attributed to e_g–e_g orbital interactions. Assuming the Jahn–Teller elongation axes are along the z-directions of each Mn^{III} ion, the $d_{x^2-y^2}$ orbitals would be empty and the d_{z^2} magnetic orbital would have a nonzero overlap with an empty $d_{x^2-y^2}$ orbital on the neighboring Mn^{III} ion through an alkoxide ligand (see Figure 2 in ref 29a). It is this $d_{x^2-y^2}/d_{z^2}$ overlap that provides an effective pathway for ferromagnetic coupling between Mn^{III} ions.[29] Therefore, the signs of the coupling constants result in an outer ring of ferromagnetically coupled Mn^{III} ions (S_{outer} = $^{24}/_2$) that are antiferromagnetically coupled to the central S_{center} = $^5/_2$ Mn^{II} ion yielding an S = $^{19}/_2$ ground state. It is thus the stronger ferromagnetic interactions that stabilize the sizable spin ground state in **2**. However, the weaker antiferromagnetic coupling, J_1, between the outer Mn^{III} spins and the central Mn^{II} suggests that there could be low-lying excited spin states. Indeed, our very simple simulation procedure suggests that the first such excited state with S = $^{21}/_2$ lies only ~5–6 cm^{-1} above the S = $^{19}/_2$ ground state. However, we wish to emphasize that this represents a rather crude estimate given the approximations employed in the simulations and further discussion with regard to the magnitude of the spin ground state will be discussed in the EPR section. As we shall see below, the AC susceptibility and EPR data presented suggest that the ground state is reasonably well isolated, i.e., it is unlikely that there are low-lying states within ~10 cm^{-1} of the ground state. Finally, we note that the obtained g-value is unphysical, in that it is larger than 2.00. Again, we shall see below that the EPR data provide a far more rigorous determination of g and the spin value associated with the ground state. The unphysical g-value can have many explanations, including torqueing of the microcrystallites in the powder sample and incorporation of impurities or solvent loss from the sample.

To further gauge the ground-state spin value and the magnitude of the zero-field splitting parameter (D), variable-field magnetization data were collected on a polycrystalline sample of **2** (suspended in eicosane) at 2–4 K with applied magnetic fields of 3–60 kG.[30] A plot of $M/N\beta$ versus H/T (reduced magnetization) for complex **2** is given in Figure 4, where M is the magnetization, N is Avogadro's number, β is the Bohr magneton, and H/T is the ratio of the magnetic field to the absolute temperature. The experimental data were fit (solid red lines in Figure 4) via full-matrix diagonalization employing eq 2, with fit parameters of S = $^{19}/_2$, g = 2.19, and D = −0.16 cm^{-1}.

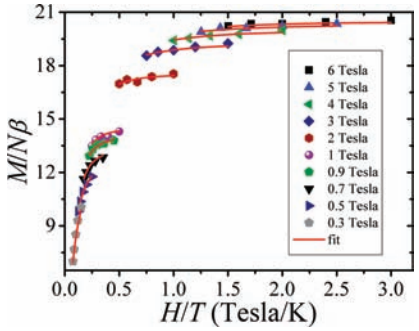

Figure 4. Reduced magnetization of complex **2** measured with a magnetic field of 0.3–6 T in the temperature range of 2–4 K. Red lines represent a best theoretical fit to the experimental data, with fitting parameters of S = $^{19}/_2$, g = 2.19, and D = −0.16 cm^{-1}.

$$M = \frac{\sum_{i=-S}^{S}(\partial E_i/\partial H)\exp[-E_i/(kT)]}{\sum_{i=-S}^{S}\exp[-E_i/(kT)]} \quad (2)$$

As we shall see below, the obtained D value agrees remarkably well with the more-precise EPR measurements. The obtained g-value is again rather high, which likely signifies torqueing of the sample, given that the effect is more extreme in the higher-field magnetization measurements. The relatively small value of the zero-field splitting parameter (D) can be rationalized by careful examination of the crystal structure. The single-ion zfs tensors of the Mn ions project onto the molecular anisotropy axis and combine to give the molecular zfs.[31] The source of the molecular zfs for complex **2** originates from the Jahn–Teller axes of the six Mn^{III} cations (one would expect only a very minor contribution from d^5 Mn^{II} ions). The six Jahn–Teller elongation axes lie along N(1)–Mn(2)–O(8) #1, N(2)–Mn(3)–O(2), N(3)–Mn(4)–O(5) bonds, and their inversion-symmetry-related pairs; they are topologically arranged in a propeller-like fashion and are tilted quite close to the Mn_7 molecular plane (see Figure 1b). Symmetry considerations would suggest that the molecular z-axis is orthogonal to the molecular plane. Given that the Jahn–Teller axes are tilted rather close to this plane, one would not expect a very significant projection of the zfs associated with the Mn^{III} ions onto the molecular z-axis. This likely explains the rather small molecular D value determined from these investigations.

AC Magnetic Susceptibility. To study magnetization relaxation behavior in complex **2**, frequency-dependent AC magnetic susceptibility measurements were performed in a 3.5 G oscillating magnetic field with frequencies of 10–10 000 Hz at temperatures ranging from 1.9–2.6 K.[32] Figure 5 shows the in-phase (top) and out-of-phase (bottom) signals plotted as magnetic susceptibility (χ_M) versus the logarithm of the frequency.

dx.doi.org/10.1021/ic2019154 | Inorg. Chem. 2012, 51, 4448–4457

Temperature- and frequency-dependent AC signals are evidence for slow magnetization relaxation and single-molecule magnet behavior, i.e., a significant thermodynamic barrier leading to magnetic bistability.

The out-of-phase component of the AC susceptibility can be used to deduce the magnitude of the kinetic barrier and the magnetization relaxation rate. The inset in Figure 5 shows a plot of the peak

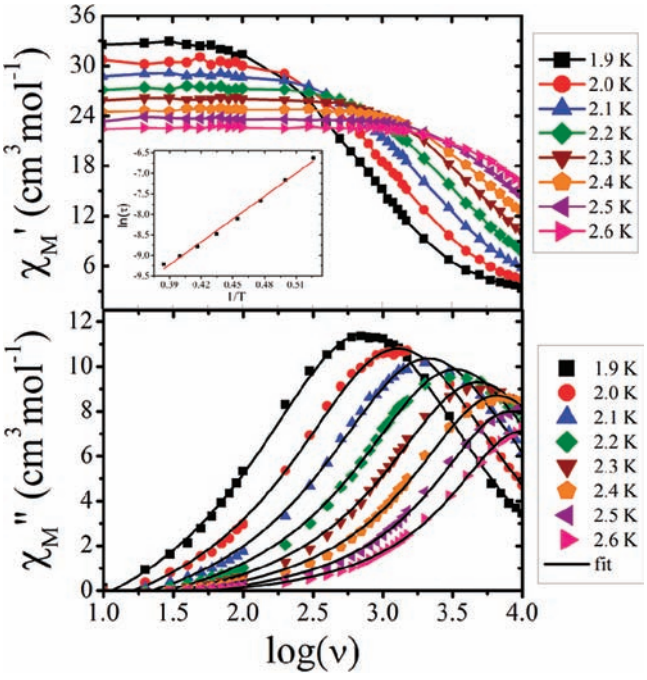

Figure 5. AC magnetic susceptibility data for complex **2** collected in a 3.5 G oscillating field with frequencies of 10–10 000 Hz in the temperature range of 1.9–2.6 K. The in-phase signals (χ_M') are presented in the top panel, and the out-of-phase signals (χ_M'') are in the bottom panel. Inset shows the Arrhenius plot; the red solid line in the inset represents the least-squares fit.

positions of the frequency-dependent out-of-phase signals plotted as ln τ vs $1/T$. The solid red line represents least-squares fitting of the experimental data to the Arrhenius formula, ln $\tau = U_{eff}/(kT) +$ ln τ_0, and yields an effective barrier of $U_{eff} = 12.9$ cm^{-1}. This value is only slightly less than the theoretical barrier, $(S_z^2 - {}^1/_4)|D| = 14.4$ cm^{-1}, determined on the basis of the magnetization fits. The difference is most likely a reflection of the uncertainty in the values determined from rather approximate methods, i.e., the magnetization fits involve approximation. However, we note that a reduction of the kinetic barrier could be caused by magnetic quantum tunneling, which would short-circuit the states near the top of the barrier. The τ_0 value obtained from the above fit is 6.97×10^{-8} s, which is quite close to two other disklike Mn_7 complexes: $[Mn^{II}_4Mn^{III}_3(teaH)_3(tea)_3](ClO_4)_2$[11] and $[Mn^{II}_3Mn^{III}_4(5\text{-}NO_2\text{-}hbide)_6]$.[17]

A Cole–Cole analysis was performed to further probe the magnetization behavior of complex **2**. Figure 6 shows the χ_M'' vs χ_M' plot at 2.1 K, where the red solid line is the theoretical fit obtained by employing eqs 3 and 4:

$$\chi_M'(\omega) = \chi_S + \frac{(\chi_T - \chi_S)\left[1 + (\omega\tau)^{1-\alpha}\sin(1/2)\alpha\pi\right]}{1 + 2(\omega\tau)^{1-\alpha}\sin(1/2)\alpha\pi + (\omega\tau)^{2(1-\alpha)}} \quad (3)$$

$$\chi_M''(\omega) = \frac{(\chi_T - \chi_S)\left[(\omega\tau)^{1-\alpha}\cos(1/2)\alpha\pi\right]}{1 + 2(\omega\tau)^{1-\alpha}\sin(1/2)\alpha\pi + (\omega\tau)^{2(1-\alpha)}} \quad (4)$$

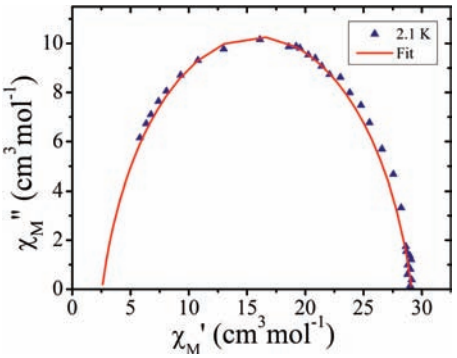

Figure 6. Cole–Cole plot at 2.1 K for complex **2**. The red solid line is the least-squares fit of the data to eqs 3 and 4.

where χ_T is the isothermal susceptibility, χ_S is the adiabatic susceptibility, and τ is the magnetization relaxation time.[33] The data and analysis suggest that the magnetization relaxation exhibited by complex **2** is not governed by a single activation process, i.e., the data in Figure 6 deviate from a perfect semicircle. A fit revealed a nonzero α-value (0.16), which indicates that there are significant distributions in the magnetization relaxation times in complex **2**. As we shall see in the following section, EPR data indicate significant disorder, which could account for a distribution of activation processes.

High-Frequency Electron Paramagnetic Resonance (HFEPR). High-frequency electron paramagnetic resonance (HFEPR) data were collected for a finely ground sample of **2** that was incorporated into a KBr pellet with frequencies of 56–216 GHz in the temperature range of 3.5–20 K. Temperature-dependent EPR spectra (collected at 216 GHz) are presented in Figure 7 (top). The two very sharp features at 3.1 and 5.6 T have been well-characterized and are attributed to paramagnetic oxygen impurities trapped in the KBr pellet. The sharp features observed around the $g = 2.00$ position (7.7 T) at elevated temperatures (15 K and above) arise because of the population of relatively isotropic excited spin ($S < {}^{19}/_2$) states. This observation may be indicative of weak coupling within the cluster and consistent with the rather small J_1 value determined from the $\chi_M T$ vs T analysis. These sharp features were ignored in our interpretation of the EPR data, and we focused instead on the broader features well away from the $g = 2.00$ position, which can be attributed to the ground spin state. We note that the temperature-dependent studies do not provide any strong indications that there are low-lying states with significant spin values (i.e., no additional peaks emerge upon raising the temperature that cannot be accounted for via simulations that assume an isolated $S = {}^{19}/_2$ ground state) (see Figure 7).

The remaining spectral features can be divided into two components: a single strong, broad feature to the high field side of $g = 2.00$; and a series of multiple features on the low field side of $g = 2.00$ that display a strong temperature dependence. For an axial system, the parallel ($H//z$) component of the powder spectrum typically extends about twice as far from the $g = 2.00$ position, compared to the perpendicular ($H\perp z$) component, with the extent of the spread being directly proportional to the magnitude of the axial D parameter. On this basis, the multiple low-field features can be attributed to resolved parallel excitations. Careful inspection of the 20 K spectrum reveals nine such peaks on the low field side of $g = 2.00$. These correspond to the following fine-structure transitions within the ground $S = {}^{19}/_2$ spin multiplet: $m_S = {}^{-19}/_2 \rightarrow {}^{-17}/_2$, $m_S = {}^{-17}/_2 \rightarrow {}^{-15}/_2$, ... and $m_S = {}^{-3}/_2 \rightarrow {}^{-1}/_2$, in order of increasing field (the ${}^{-1}/_2$ to ${}^{+1}/_2$ transition is buried in the $g = 2.00$ feature, and

dx.doi.org/10.1021/ic2019154 | Inorg. Chem. 2012, 51, 4448–4457

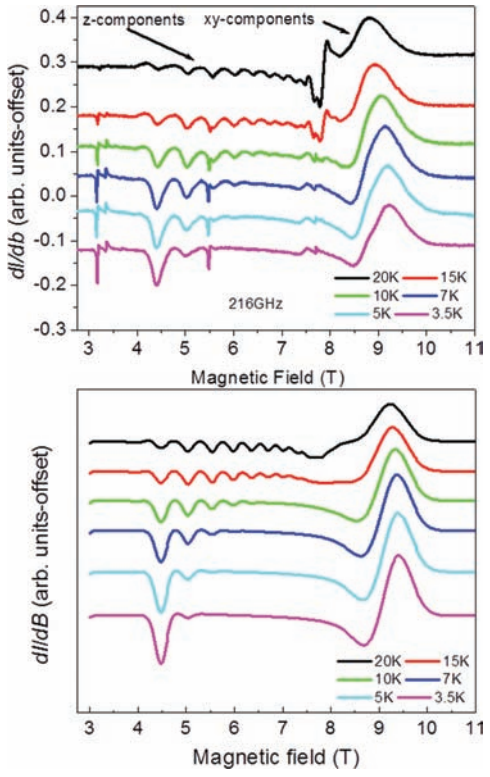

Figure 7. Temperature-dependent HFEPR spectra of complex **2** (experimental (top) and simulated (bottom)), recorded at 216 GHz in the temperature range of 3.5−20 K collected on a microcrystalline sample restrained in KBr.

the remaining ones overlap with the perpendicular portion of the spectrum). The fact that the spectral weight associated with the parallel spectrum shifts to the low field $m_S = {}^{-19}/_2 \rightarrow {}^{-17}/_2$ transition upon cooling provides confirmation of the negative sign of D, i.e., the $m_S = {}^{-19}/_2$ state is lowest in energy when $H//z$.

In contrast to the parallel spectrum, the fine structure transitions within the perpendicular spectrum were not resolved. There are several possible reasons for this. First, the relevant peaks should have been much more closely spaced (i.e., two perpendicular components, each with half the separation of the parallel spectrum) and, therefore, more difficult to resolve. Nevertheless, this alone cannot fully account for the observed spectrum. A likely explanation is molecular disorder and/or strains in the sample that affect the transverse zero-field splitting parameters (e.g., E) more than the axial parameter (D). This type of disorder is known to occur in the extensively studied Mn_{12}-acetate SMM,[34] where such strains have been shown to wash out the perpendicular spectrum without affecting the parallel spectrum significantly. It is also well-known that the crystallites in powdered SMM samples are subject to substantial torques that can cause minor reorientations of individual particles, even in well-constrained samples. Again, this effect can lead to a substantial broadening of the perpendicular spectrum and almost no effect on the parallel component. All of these influences can be taken into consideration when simulating spectra using a program such as EasySpin.[35] Figure 7 (bottom) displays such a simulation, obtained by employing the following Hamiltonian:

$$\hat{H} = \mu_B \vec{H} \cdot \vec{g} \cdot \hat{S} + D\hat{S}_z^2 + B_4^0 \hat{O}_4^0 \qquad (5)$$

where $\hat{S}$ and $\hat{S}_Z$ are spin operators, $\vec{H}$ is the applied magnetic field vector, $\vec{g}$ is the Landé g tensor, μ_B is the Bohr magneton, D is the second-order axial zero-field splitting parameter, and the final term represents axial fourth-order zero-field splitting.[35] The parameters used for the simulation were $S = {}^{19}/_2$, $D = -0.157$ cm^{-1}, $B_4^0 = -9 \times 10^{-6}$ cm^{-1}, and $g_{xy} = g_z = 2.00$. As can be seen, the relevant parallel and perpendicular portions of the simulations agree with the experiments in every respect, and the obtained D value is fully consistent with that deduced from reduced magnetization studies. The unresolved perpendicular part of the spectrum can be reproduced by introducing a Gaussian distribution of the second-order transverse zero-field anisotropies (E-strain), centered at $E = 0$, and with a full width at half maximum (fwhm) of ∼0.025 cm^{-1}. This is very similar to the situation reported for Mn_{12}acetate,[34] suggesting that disorder is responsible for the unresolved perpendicular fine structures. We note also that a Gaussian distribution (strain) of the D parameter (fwhm of 0.007 cm^{-1}) was also employed in these simulations. It should be noted that no transverse rhombic parameter (E) was included in our simulations even though this term is certainly allowed according to symmetry considerations. However, since no perpendicular fine structures could be resolved above the $g = 2$ position, we could not determine a value for E, even though we cannot rule out such molecular anisotropy.

In order to obtain tighter constraints on the spin Hamiltonian parameters for complex **2**, frequency-dependent powder EPR experiments were carried out with frequencies in the range of 56−216 GHz. The positions of the parallel component absorption peaks were then plotted versus frequency, as seen in Figure 8, and

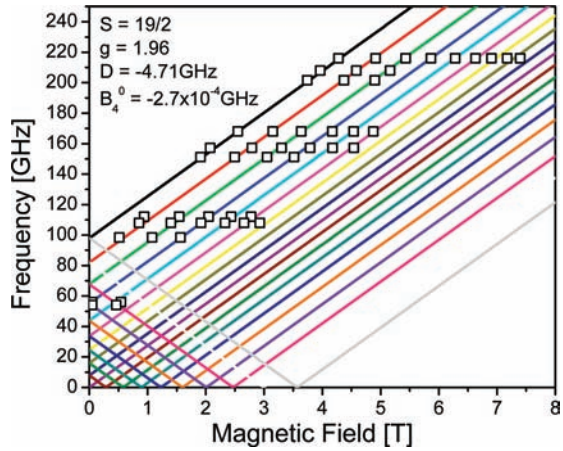

Figure 8. Easy-axis (z-axis) frequency-dependent EPR data for complex **2**. The solid lines are a simulation of the data employing the parameters: $S = {}^{19}/_2$, $g = 1.96$, $D = -4.71$ GHz (-0.16 cm^{-1}) and $B_4^0 = -2.7 \times 10^{-4}$ GHz (-9.0×10^{-6} cm^{-1}).

the data simulated with the Hamiltonian of eq 5. The solid lines in Figure 8 represent the best simulation of the frequency-dependent data using the following parameter: $S = {}^{19}/_2$, $g_z = 1.96$, $D = -0.16$ cm^{-1} and $B_4^0 = -9.0 \times 10^{-6}$ cm^{-1}. We note that the fourth-order term is absolutely essential to the simulations, accounting for the uneven spacing of the resonances. The obtained parameters agree well with those used in the simulation shown in Figure 7, and those extracted from fits of reduced magnetization data. In addition, it is possible to estimate a kinetic barrier to magnetization relaxation (U_{eff}) of 14.4 cm^{-1} from these parameters (see the Supporting Information). Again, this value is slightly larger than that deduced from AC magnetic susceptibility studies, with the difference attributable to the aforementioned tunneling near the top of the barrier. Though the EPR simulation parameters agree well with those obtained through magnetic reduced magnetization

dx.doi.org/10.1021/ic2019154 | Inorg. Chem. 2012, 51, 4448−4457

simulations, we note that one can also achieve reasonable simulations with other spin values (e.g., $^{17}/_2$ or $^{21}/_2$), together with correspondingly adjusted ZFS parameters. We would like to point out, however, that no simple exchange scheme can be envisioned that would yield a ground state spin value different from $^{19}/_2$, while simultaneously accounting for all of the experimental observations. A ferromagnetic coupled outer ring of Mn^{III} ions ($S_0 = {}^{24}/_2$) coupled antiferromagnetically to the central Mn^{II} ($S_c = {}^5/_2$) ion yields an $S = {}^{19}/_2$ ground state. To obtain a different ground state spin value for this cluster topology would require the introduction of competing/frustrating interactions, likely resulting in many low-lying spin states that are not observed in the EPR spectra.

We conclude this section by returning to the issue of the perpendicular EPR spectrum and the suggestion that this may be due to disorder. Such an explanation is actually rather plausible given the propeller-like arrangements of the Mn^{III} Jahn−Teller axes. The approximate hexagonal/axial symmetry of the cluster ensures that any projection of the Mn^{III} anisotropies perpendicular to the plane of the molecule will add. In contrast, the projections within the plane will cancel. If one then introduces disorder, its effect will be far more severe in terms of the projections within the plane. This is easy to see if one considers a perfect hexagonal symmetry where the transverse second-order anisotropy would exactly cancel. Introduction of disorder would thus generate a distribution of transverse anisotropies, which is clearly a rather dramatic deviation from zero transverse anisotropy. Moreover, because the Jahn−Teller axes are tilted rather close to the molecular plane in the case of **2**, this effect could be rather severe. In contrast, disorder would merely generate a small distribution of longitudinal anisotropies around the undistorted value. It should be emphasized that this phenomenology is not at all new and has been studied and discussed in considerable detail in the context of the high-symmetry Mn_{12} SMMs.[36] Even more important is the fact that the transverse anisotropy provides a rather efficient mechanism for short-circuiting states close to the top of the barrier via tunneling, thus reducing the kinetic magnetization relaxation barrier. Hence, a distribution of transverse anisotropies also provides a natural explanation for the distribution of relaxation times deduced from the Cole−Cole analysis of the AC susceptibility data. Indeed, the value of α (0.16) obtained from analysis of the complex AC susceptibility data is very similar to the value found for Mn_{12}BrAc ($\alpha = 0.15$).[37] This variant of Mn_{12} contains a highly volatile solvent of crystallization and is, thus, highly susceptible to being disordered as a result of loss of solvent molecules. Recent studies have shown that this can give rise to a distribution of relaxation barriers due to below barrier tunneling, exactly as proposed here.[36]

Comparisons of Disklike Mn_7 Complexes. There are many reports of disklike heptanuclear clusters with different first-row transition metals in the literature.[38] In part, this structure arises because of the packing of the metal/oxygen cores, which are nearly structurally identical to layered metal oxides such as the mineral litiophorite. In our literature survey, we found 13 compounds with nearly structurally identical hepta-manganese cores that differ mainly in the oxidation states and distribution of the Mn ions. All of these compounds and their ligands are listed in Table 3, top and bottom, respectively. These compounds can be easily classified into three categories, according to their oxidation states, i.e., $Mn^{II}_4Mn^{III}_3$, Mn^{II}_7, and $Mn^{II}_3Mn^{III}_4$. The arrangements of the metal/oxygen cores of these three categories are illustrated in Figures 9a−c.

Table 3. Comparisons of Disklike Mn_7 Complexes

complex	ref	S	D (cm^{-1})	U_{eff} (K)
$[Mn^{II}_4Mn^{III}_3(OH)_3(hmp)_9Cl_3](Cl)(ClO_4)$	10	11	−0.11	
$[Mn^{II}_4Mn^{III}_3(teaH)_3(tea)_3](ClO_4)_2\cdot 3MeOH$	11	11	−0.08	19.5
$[NEt_4]\{Mn^{II}[Mn^{II}_3Mn^{III}_3Cl_6(mda)_6]\}$	12			
$\{[Na(MeOH)_3][Mn^{II}_4Mn^{III}_3(N_3)_6(mda)_6]\}_n$	13	11	−0.15	
$(NHEt_3)[Mn^{II}_4Mn^{III}_3Cl_6(mda)_6]$	14	11	−0.13	
$(NHEt_3)[Mn^{II}_4Mn^{III}_3(N_3)_6(mda)_6]$	14	11		
$\{Na[Mn^{II}_4Mn^{III}_3(N_3)_6(teaH)_6]\}_n$	13	16	−0.02	
$(NHEt_3)[Mn^{II}_4Mn^{III}_3(N_3)_6(teaH)_6]$	14	16		
$[Mn^{II}_7(pppd)_6(tea)(OH)_3][BF_4]_2\cdot 2MeOH\cdot 2CH_2Cl_2$	15	$^5/_2$		
$[Mn^{II}_7(paa)_6(OMe)_6][NO_3]_2\cdot 6MeOH$	15	$^5/_2$		
$[Mn^{II}_3Mn^{III}_4(OMe)_{12}(dbm)_6]\cdot CHCl_3\cdot 14MeOH$	16	$^{17}/_2$	−0.27	
$[Mn^{II}_3Mn^{III}_4(5\text{-}NO_2\text{-}hbide)_6]\cdot 5C_2H_4Cl_2$	17	$^{19}/_2$	−0.20	18.1
$\{Mn^{II}[Mn^{II}_2Mn^{III}_4Cl_6(L^3)_6]\}\cdot 2CHCl_3$	18	$^{27}/_2$	−0.05	10

ligand	chemical name
Hhmp	2-hydroxymethylpyridine
$teaH_3$	triethanolaminate
$mdaH_2$	*N*-methyldiethanolamine
pppdH	1-phenyl-3-(2-pyridyl)propane-1,3-dione
paaH	*N*-(2-pyridinyl)acetoacetamide
Hdbm	dibenzoylmethane
$H_3(5\text{-}NO_2\text{-}hbide)$	*N*-(2-hydroxy-5-nitrobenzyl)iminodiethanol
H_2L^3	*N*-*n*-butyldiethanolamine

In the first class, $Mn^{II}_4Mn^{III}_3$, the structure contains an outer ring of alternating Mn^{II} and Mn^{III} ions that encircle the central Mn^{II} ion (see Figure 9a). All but two of these compounds possess spin ground states of $S = 11$, with two compounds possessing an $S = 16$ spin ground state. In the $S = 11$ case, the spins that form the peripheral ring are ferromagnetically coupled leading to parallel arrangements, but they are antiferromagnetically coupled to the central Mn^{II} ion. Small structural distortions lead to ferromagnetic interactions between the spins on the peripheral ring and the central Mn^{II} ion leading to an $S = 16$ ground state. Only one compound ($[Mn^{II}_4Mn^{III}_3(teaH)_3(tea)_3](ClO_4)_2\cdot 3MeOH$)[11] in this series was reported to show relaxation behavior, with a molecular zfs of $D \approx -0.08$ cm^{-1} and a kinetic energy barrier (U_{eff}) of 19.5 K.

In the second category, all seven of the Mn ions are $S = {}^5/_2$ high-spin d^5 Mn^{II} ions (see Figure 9b). This series of complexes is dominated by strong antiferromagnetic interactions between neighboring Mn^{II} ions that, because of an odd number of magnetic ions, leads to an $S = {}^5/_2$ ground state. Not surprisingly, no complexes of the series were shown to exhibit SMM behavior. This is not unexpected when one considers the relatively isotropic nature of Mn^{II} ions.

The third series in this topology are shown in Figure 9c. Structurally, they have a linear arrangement of three Mn^{II} ions that pass through the center of the complex, with two Mn^{III} ions located on either side (see Figure 9c). These complexes possess $Mn^{II}_3Mn^{III}_4$ configurations and, therefore, an odd number of valence electrons, which leads to half-integer spin systems with $S = {}^{17}/_2$, $^{19}/_2$, and $^{27}/_2$ ground states, respectively.[16−18] Moreover, in contrast to the first two series of molecules with similar molecular topologies, no simple model can be constructed with regard to the type (antiferromagnetic or ferromagnetic) of intramolecular magnetic exchange interactions that will simply yield the observed spin ground states

dx.doi.org/10.1021/ic2019154 | *Inorg. Chem.* 2012, 51, 4448−4457

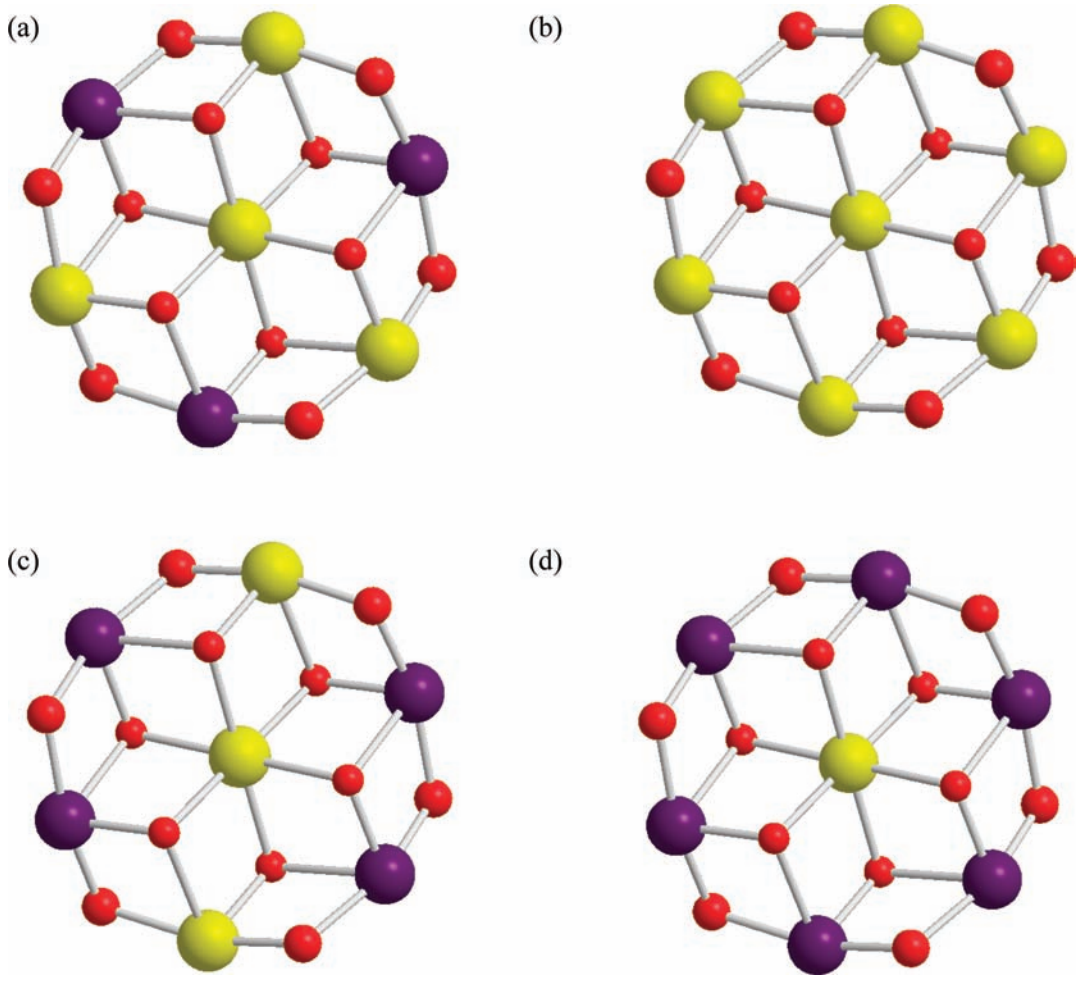

Figure 9. Illustrations of Mn/O cores in all disklike Mn_7 complexes: Mn^{II}, yellow; Mn^{III}, purple; O, red: (a) $Mn^{II}_4Mn^{III}_3$, (b) Mn^{II}_7, (c) $Mn^{II}_3Mn^{III}_4$, and (d) $Mn^{II}Mn^{III}_6$ (current paper).

of these complexes. As a result of the spacial arrangement of the magnetic ions, these complexes possess appreciably spin-frustrated magnetic cores that lead to complicated spin ground states, as extensively studied in exchange-coupled trinuclear compounds.[39] The $S = {}^{19}/_2$ and $S = {}^{27}/_2$ complexes were both shown to exhibit slow magnetization relaxation behavior consistent with SMMs with significant barriers toward magnetization reversal (U_{eff}) of 18.1 and 10 K, respectively.

In the present study, a new ligand system was developed ($heampH_3$) that, because of charge considerations and constraints imposed by the structure of the peripheral $heamp^{3-}$ ligand, leads to an unprecedented oxidation state configuration of $Mn^{II}Mn^{III}_6$ (see Figure 9d) that has previously not been seen for this topology. It is clear that very subtle changes in structural parameters and oxidation state arrangements can have a significant influence on exhibited magnetic properties. As a case in point, only a select few of these complexes have been shown to exhibit magnetic bistability.

CONCLUSION

A new heptanuclear manganese cluster with half-integer spin ($S = {}^{19}/_2 \pm 1$) was synthesized and studied employing crystallographic, magnetic susceptibility, and high-frequency electron paramagnetic resonance (HFEPR) techniques. In our survey, we identified 13 previously reported disklike Mn_7 metal clusters; however, only three of these complexes exhibit slow magnetic relaxation behavior.[11,17,18] The hexagonal disklike topology is interesting, because synthetic versatility yields both integer and half-integer spin ground states, and the different arrangements of manganese oxidation states lead to extremely different magnetic properties. The previously reported complexes have electron configurations of $Mn^{II}_4Mn^{III}_3$, Mn^{II}_7, and $Mn^{II}_3Mn^{III}_4$. However, complex **2** has a $Mn^{II}Mn^{III}_6$ arrangement that has not been reported previously. AC susceptibility studies show that this complex exhibits slow magnetization relaxation, and HFEPR studies indicate that complex **2** possesses an $S = {}^{19}/_2 \pm 1$ ground state and exhibits negative axial-type magnetoanisotropy ($D = -0.16$ cm^{-1}), clearly showing that complex **2** is a single-molecule magnet (SMM). AC and HFEPR studies also reveal that complex **2** possesses a significant relaxation barrier ($U_{eff} = 12.9$ cm^{-1}) that is smaller than the theoretical barrier ($(S_z^2 - {}^1/_4)|D| = 14.4$ cm^{-1}), and that the smaller effective barrier is probably the result of quantum tunneling near the top of the barrier.

ASSOCIATED CONTENT

Supporting Information

The Bond-Valence-Sum calculations, the CIF file, and the tables for crystallographic data are available free of charge via the Internet at http://pubs.acs.org.

dx.doi.org/10.1021/ic2019154 | Inorg. Chem. 2012, 51, 4448–4457

AUTHOR INFORMATION

Corresponding Author

*Tel.: 850 644 1647 (S.H.), +886-2-2905-3571 (E.-C.Y.). E-mails: shill@magnet.fsu.edu (S.H.), 071549@mail.fju.edu.tw (E.-C.Y.).

Notes

The authors declare no competing financial interest.

ACKNOWLEDGMENTS

The authors thank Professor Hui-Lien Tsai (National Cheng Kung University) for assistance with the AC measurements. This work was supported by the National Science Council of Taiwan (No. NSC98-2113-M-030-003-MY2). A portion of this work was performed at the National High Magnetic Field Laboratory, which is supported by National Science Foundation (NSF) Cooperative Agreement No. DMR-0654118, the State of Florida. S.H. and C.B. also acknowledge the support of an NSF (Grant Nos. DMR0804408 and CHE0924374). C.B. also acknowledges funding from the Florida State University Schuler Postdoctoral Fellowship.

REFERENCES

(1) (a) Christou, G. *Acc. Chem. Res.* **1989**, *22*, 328. (b) *Manganese Redox Enzymes*; Pecoraro, V. L., Ed.; VCH Publishers: New York, 1992.

(2) (a) Caneschi, A.; Gatteschi, D.; Sessoli, R.; Barra, A. L.; Brunel, L. C.; Guillot, M. *J. Am. Chem. Soc.* **1991**, *113*, 5873. (b) Aubin, S. M. J.; Dilley, N. R.; Pardi, L.; Krzystek, J.; Wemple, M. W.; Brunel, L.-C.; Maple, M. B.; Christou, G.; Hendrickson, D. N. *J. Am. Chem. Soc.* **1998**, *120*, 4991. (c) Christou, G.; Gatteschi, D.; Hendrickson, D. N.; Sessoli, R. *MRS Bull.* **2000**, *25* (11), 66. (d) Gatteschi, D.; Sessoli, R. *Angew. Chem., Int. Ed.* **2003**, *42*, 268. (e) Oshio, H.; Nakano, M. *Chem.—Eur. J.* **2005**, *11*, 5178. (f) Bircher, R.; Chaboussant, G.; Dobe, C.; Güdel, H. U.; Ochsenbein, S. T.; Sieber, A.; Waldmann, O. *Adv. Funct. Mater.* **2006**, *16*, 209. (g) Aromí, G.; Brechin, E. K. *Struct. Bonding (Berlin)* **2006**, *122*, 1. (h) Powell, A. K. *Nat. Chem.* **2010**, *2*, 351.

(3) (a) Heersche, H. B.; de Groot, Z.; Folk, J. A.; van der Zant, H. S. J.; Romeike, C.; Wegewijs, M. R.; Zobbi, L.; Barreca, D.; Tondello, E.; Cornia, A. *Phys. Rev. Lett.* **2006**, *96*, 206801. (b) Jo, M. H.; Grose, J. E.; Baheti, K.; Deshmukh, M. M.; Sokol, J. J.; Rumberger, E. M.; Hendrickson, D. N.; Long, J. R.; Park, H.; Ralph, D. C. *Nano Lett.* **2006**, *6*, 2014. (c) Wernsdorfer, W. *Nat. Mater.* **2007**, *6*, 174. (d) Bogani, L.; Wernsdorfer, W. *Nat. Mater.* **2008**, *7*, 179. (e) Roch, N.; Florens, S.; Bouchiat, V.; Wernsdorfer, W.; Balestro, F. *Nature* **2008**, *453*, 633. (f) Wernsdorfer, W. *Nat. Nanotechnol.* **2009**, *4*, 145.

(4) (a) Leuenberger, M. N.; Loss, D. *Nature* **2001**, *410*, 789. (b) Meier, F.; Levy, J.; Loss, D. *Phys. Rev. Lett.* **2003**, *90*, 047901. (c) Tejada, J.; Chudnovsky, E. M.; del Barco, E.; Hernandez, J. M.; Spiller, T. P. *Nanotechnology* **2001**, *12* (2), 181.

(5) (a) Gatteschi, D.; Caneschi, A.; Pardi, L.; Sessoli, R. *Science* **1994**, *265*, 1054. (b) Gunther, L., Barbara, B., Eds. *Quantum Tunneling of Magnetization: QTM '94*; NATO ASI Series E, Applied Sciences, No. 301; Kluwer Academic Publishers: Boston, 1995. (c) Friedman, J. R.; Sarachik, M. P.; Tejada, J.; Ziolo, R. *Phys. Rev. Lett.* **1996**, *76*, 3830. (d) Thomas, L.; Lionti, F.; Ballou, R.; Gatteschi, D.; Sessoli, R.; Barbara, B. *Nature* **1996**, *383*, 145. (e) Tejada, J.; Ziolo, R. F.; Zhang, X. X. *Chem. Mater.* **1996**, *8*, 1784.

(6) (a) Ramsey, C. M.; del Barco, E.; Hill, S.; Shah, S. J.; Beedle, C. C.; Hendrickson, D. N. *Nat. Phys.* **2008**, *4*, 277. (b) Wernsdorfer, W.; Sessoli, R. *Science* **1999**, *284*, 133. (c) Wernsdorfer, W.; Soler, M.; Christou, G.; Hendrickson, D. N. *J. Appl. Phys.* **2002**, *91*, 7164. (d) Waldmann, O.; Stamatatos, T. C.; Christou, G.; Güdel, H. U.; Sheikin, I.; Mutka, H. *Phys. Rev. Lett.* **2009**, *102*, 157202.

(7) (a) Friedman, J. R.; Sarachik, M. P.; Tejada, J.; Maciejewski, J.; Ziolo, R. *J. Appl. Phys.* **1996**, *79*, 6031. (b) Wernsdorfer, W.; Aliaga-Alcalde, N.; Hendrickson, D. N.; Christou, G. *Nature* **2002**, *416*, 406. (c) Yang, E. C.; Wernsdorfer, W.; Hill, S.; Edwards, R. S.; Nakano, M.; Maccagnano, S.; Zakharov, L. N.; Rheingold, A. L.; Christou, G.; Hendrickson, D. N. *Polyhedron* **2003**, *22* (14−17), 1727.

(8) (a) Gomes, A. M.; Novak, M. A.; Wernsdorfer, W.; Sessoli, R.; Sorace, L.; Gatteschi, D. *J. Appl. Phys.* **2000**, *87*, 6004. (b) Wernsdorfer, W.; Bhaduri, S.; Boskovic, C.; Christou, G.; Hendrickson, D. N. *Phys. Rev. B* **2002**, *65*, 180403. (c) Wernsdorfer, W.; Chakov, N. E.; Christou, G. *Phys. Rev. Lett.* **2005**, *95*, 037203.

(9) (a) Hill, S.; Edwards, R. S.; Aliaga-Alcalde, N.; Christou, G. *Science* **2003**, *302* (5647), 1015. (b) Takahashi, S.; Tupitsyn, I. S.; van Tol, J.; Beedle, C. C.; Hendrickson, D. N.; Stamp, P. C. E. *Nature* **2011**, *476* (7358), 76. (c) Takahashi, S.; van Tol, J.; Beedle, C. C.; Hendrickson, D. N.; Brunel, L.-C.; Sherwin, M. S. *Phys. Rev. Lett.* **2009**, *102* (8), 087603. (d) Chudnovsky, E. M.; Friedman, J. R. *Phys. Rev. Lett.* **2000**, *85* (24), 5206. (e) Luis, F.; Mettes, F. L.; Tejada, J.; Gatteschi, D.; de Jongh, L. J. *Phys. Rev. Lett.* **2000**, *85* (20), 4377.

(10) (a) Harden, N. C.; Bolcar, M. A.; Wernsdorfer, W.; Abboud, K. A.; Streib, W. E.; Christou, G. *Inorg. Chem.* **2003**, *42*, 7067. (b) Bolcar, M. A.; Aubin, S. M. J.; Folting, K.; Hendrickson, D. N.; Christou, G. *Chem. Commun.* **1997**, 1485.

(11) Pilawa, B.; Kelemen, M. T.; Wanka, S.; Geisselmann, A.; Barra, A. L. *Europhys. Lett.* **1998**, *43*, 7.

(12) Saalfrank, R. W.; Nakajima, T.; Mooren, N.; Scheurer, A.; Maid, H.; Hampel, F.; Trieflinger, C.; Daub, J. *Eur. J. Inorg. Chem.* **2005**, 1149.

(13) Stamatatos, T. C.; Poole, K. M.; Foguet-Albiol, D.; Abboud, K. A.; O'Brien, T. A.; Christou, G. *Inorg. Chem.* **2008**, *47*, 6593.

(14) Stamatatos, T. C.; Foguet-Albiol, D.; Poole, K. M.; Wernsdorfer, W.; Abboud, K. A.; O'Brien, T. A.; Christou, G. *Inorg. Chem.* **2009**, *48*, 9831.

(15) Langley, S. K.; Chilton, N. F.; Massi, M.; Moubaraki, B.; Berry, K. J.; Murray, K. S. *Dalton Trans.* **2010**, *39*, 7236.

(16) Abbati, G. L.; Cornia, A.; Fabretti, A. C.; Caneschi, A.; Gatteschi, D. *Inorg. Chem.* **1998**, *37*, 3759.

(17) (a) Koizumi, S.; Nihei, M.; Shiga, T.; Nakano, M.; Nojiri, H.; Bircher, R.; Waldmann, O.; Ochsenbein, S. T.; Güdel, H. U.; Fernandez-Alonso, F.; Oshio, H. *Chem.—Eur. J.* **2007**, *13*, 8445. (b) Koizumi, S.; Nihei, M.; Nakano, M.; Oshio, H. *Inorg. Chem.* **2005**, *44*, 1208.

(18) Saalfrank, R. W.; Scheurer, A.; Prakash, R.; Heinemann, F. W.; Nakajima, T.; Hampel, F.; Leppin, R.; Pilawa, B.; Rupp, H.; Müller, P. *Inorg. Chem.* **2007**, *46*, 1586.

(19) (a) Wu, C.-C.; Datta, S.; Wernsdorfer, W.; Lee, G.-H.; Hill, S.; Yang, E.-C. *Dalton Trans.* **2010**, *39*, 10160. (b) Chen, Y.-H.; Tsai, Y.-F.; Lee, G.-H.; Yang, E.-C. *J. Solid State Chem.* **2012**, *185*, 166−171.

(20) Vincent, J. B.; Chang, H.-R.; Folting, K.; Huffman, J. C.; Christou, G.; Hendrickson, D. N. *J. Am. Chem. Soc.* **1987**, *109*, 5703.

(21) *Sadabs*: Sheldrick, G. M. 2002, Version 2.03, University of Göttingen, Göttingen, Germany.

(22) Sheldrick, G. M. SHELXS-97. *Acta Crystallogr., Sect. A: Found. Crystallogr.* **1990**, *A46*, 467.

(23) Sheldrick, G. M. *SHELXL-97*; University of Göttingen: Göttingen, Germany, 1997.

(24) Hassan, A. K.; Pardi, L. A.; Krzystek, J.; Sienkiewicz, A.; Goy, P.; Rohrer, M.; Brunel, L.-C. *J. Magn. Reson.* **2000**, *142* (2), 300.

(25) (a) Brown, I. D.; Altermatt, D. *Acta Crystallogr., Sect. B: Struct. Sci.* **1985**, *B41*, 244. (b) Liu, W.; Thorp, H. H. *Inorg. Chem.* **1993**, *32*, 4102.

(26) (a) Hill, S.; Datta, S.; Liu, J.; Inglis, R.; Milios, C. J.; Feng, P. L.; Henderson, J. J.; del Barco, E.; Brechin, E. K.; Hendrickson, D. N. *Dalton Trans.* **2010**, *39*, 4693−4707. (b) Inglis, R.; Houton, E.; Liu, J.; Prescimone, A.; Cano, J.; Piligkos, S.; Hill, S.; Jones, L. F.; Brechin, E. K. *Dalton Trans.* **2011**, *40*, 9999−10006.

(27) Kambe, K. *J. Phys. Soc. Jpn.* **1950**, *5*, 48.

(28) (a) Borrás-Almenar, J. J.; Clemente-Juan, J. M.; Coronado, E.; Tsukerblat, B. S. *Inorg. Chem.* **1999**, *38*, 6081. (b) Borrás-Almenar, J. J.; Clemente-Juan, J. M.; Coronado, E.; Tsukerblat, B. S. *J. Comput. Chem.* **2001**, *22*, 985.

(29) (a) Abbati, G. L.; Cornia, A.; Fabretti, A. C.; Caneschi, A.; Gatteschi, D. *Inorg. Chem.* **1998**, *37*, 1430. (b) Ginsberg, A. P. *Inorg. Chim. Acta Rev.* **1971**, *5*, 45.
(30) Yoo, J.; Yamaguchi, A.; Nakano, M.; Krzystek, J.; Streib, W. E.; Brunel, L.-C.; Ishimoto, H.; Christou, G.; Hendrickson, D. N. *Inorg. Chem.* **2001**, *40*, 4604.
(31) (a) Gatteschi, D.; Sorace, L. *J. Solid State Chem.* **2001**, *159* (2), 253. (b) Boča, R. *Theoretical Foundations of Molecular Magnetism*; Elsevier: New York, 1999.
(32) Carlin, R. L. *Magnetochemistry*; Springer−Verlag: Berlin, Heidelberg, 1986.
(33) (a) Aubin, S. M. J.; Sun, Z.; Pardi, L.; Krzysteck, J.; Folting, K.; Brunel, L.-C.; Rheingold, A. L.; Christou, G.; Hendrickson, D. N. *Inorg. Chem.* **1999**, *38*, 5329. (b) Cole, K. S.; Cole, R. H. *J. Chem. Phys.* **1941**, *9*, 341.
(34) (a) Hill, S.; Edwards, R. S.; Jones, S. I.; Dalal, N. S.; North, J. M. *Phys. Rev. Lett.* **2003**, *90* (21), 217204. (b) Hill, S.; Maccagnano, S.; Achey, R.; Dalal, N.; Park, K. *Int. J. Mod. Phys. B* **2002**, *16* (20−22), 3326. (c) Park, K.; Novotny, M. A.; Dalal, N. S.; Hill, S.; Rikvold, P. A. *Phys. Rev. B.* **2002**, *65* (1), 014426.
(35) Stoll, S.; Schweiger, A. *J. Magn. Reson.* **2006**, *178* (1), 42.
(36) (a) Hill, S.; Murugesu, M.; Christou, G. *Phys. Rev. B* **2009**, *80*, 174416. (b) Redler, G.; Lampropoulos, C.; Datta, S.; Koo, C.; Stamatatos, T. C.; Chakov, N. E.; Christou, G.; Hill, S. *Phys. Rev. B* **2009**, *80*, 094408.
(37) Chakov, N. E.; Lee, S. C.; Harter, A. G.; Kuhns, P. L.; Reyes, A. P.; Hill, S. O.; Dalal, N. S.; Wernsdorfer, W.; Abboud, K. A.; Christou, G. *J. Am. Chem. Soc.* **2006**, *128*, 6975.
(38) (a) Hoshino, N.; Ako, A. M.; Powell, A. K.; Oshio, H. *Inorg. Chem.* **2009**, *48*, 3396. (b) Chibotaru, L. F.; Ungur, L.; Aronica, C.; Elmoll, H.; Pilet, G.; Luneau, D. *J. Am. Chem. Soc.* **2008**, *130*, 12445. (c) Zhang, S.-H.; Ma, L.-F.; Zou, H.-H.; Wang, Y.-G.; Liang, H.; Zeng, M.-H. *Dalton Trans.* **2011**, *40*, 11402. (d) Meally, S. T.; McDonald, C.; Karotsis, G.; Papaefstathiou, G. S.; Brechin, E. K.; Dunne, P. W.; McArdle, P.; Power, N. P.; Jones, L. F. *Dalton Trans.* **2010**, *39*, 4809. (e) Wei, L.-Q.; Zhang, K.; Feng, Y.-C.; Wang, Y.-H.; Zeng, M.-H.; Kurmoo, M. *Inorg. Chem.* **2011**, *50*, 7274−7283. (f) Tesmer, M.; Müller, B.; Vahrenkamp, H. *Chem. Commun.* **1997**, 721. (g) Zhang, S.-H.; Feng, C. *J. Mol. Struct.* **2010**, *977*, 62.
(39) (a) McCusker, J. K.; Jang, H. G.; Wang, S.; Christou, G.; Hendrickson, D. N. *Inorg. Chem.* **1992**, *31*, 1874. (b) McCusker, J. K.; Vincent, J. B.; Schmitt, E. A.; Mino, M. L.; Shin, K.; Coggin, D. K.; Hagen, P. M.; Huffman, J. C.; Christou, G.; Hendrickson, D. N. *J. Am. Chem. Soc.* **1991**, *113*, 3012.

dx.doi.org/10.1021/ic2019154 | *Inorg. Chem.* 2012, 51, 4448−4457